POLITECNICO DI TORINO
Repository ISTITUZIONALE

Response of reinforced concrete beams subjected to debris impact: A simplified model

Original
Response of reinforced concrete beams subjected to debris impact: A simplified model / Zeinali Miankooh, E., Kiakojouri, F., De Biagi, V.. - In: ENGINEERING FAILURE ANALYSIS. - ISSN 1350-6307. - 178:(2025), pp. 1-20. [10.1016/j.engfailanal.2025.109661]

Availability:
This version is available at: 11583/3001247 since: 2025-07-03T11:24:12Z

Publisher:
Elsevier

Published
DOI:10.1016/j.engfailanal.2025.109661

Terms of use:

This article is made available under terms and conditions as specified in the corresponding bibliographic description in the repository

Publisher copyright

(Article begins on next page)

09 November 2026

Engineering Failure Analysis 178 (2025) 109661

Contents lists available at ScienceDirect

Engineering Failure Analysis

journal homepage: www.elsevier.com/locate/engfailanal

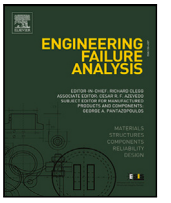

Response of reinforced concrete beams subjected to debris impact: A simplified model

Elahe Zeinali, Foad Kiakojouri, Valerio De Biagi *

Department of Structural, Geotechnical and Building Engineering (DISEG) - Politecnico di Torino, Torino, Italy

ARTICLE INFO

Keywords:
Impact
Reinforced concrete beams
Falling debris
Progressive collapse
Analytical model

ABSTRACT

Recent research on progressive collapse has predominantly focused on redistributional mechanisms, where load paths are reestablished following the failure of critical members. However, many notable structural failures are governed by impact-type progressive collapse mechanisms, which remain less understood. To address this gap, this study develops a novel analytical model designed to study the dynamic interactions between impacting bodies and reinforced concrete (RC) beams. The model utilizes a mass–spring–damper system and introduces a dynamically recalculated equivalent mass. This advancement enables highly accurate predictions of contact forces, showing up improvements in accuracy compared to existing methods. A comprehensive parametric analysis was conducted, investigating the effects of critical variables such as the impactor's mass, velocity, and beam length. Among these, the velocity of the impactor was identified as the dominant factor that influences structural response, with significant implications for energy dissipation and failure progression. The results underscore the complex interplay between dynamic effects and structural properties, offering valuable insights into failure mechanisms under real-world impact conditions.

1. Introduction

The progressive collapse is a set of physical and mechanical phenomena that let a damage to propagate from a local state, e.g. a single or a couple of structural members, to a final state for which the failure interests the whole structural system [1]. The damage progression is a chain-like effect for which there is a release of energy, either internal or potential, from an initial stage to a final situation [2]. Although the mechanisms for damage propagation are multiple and depend on the type of structure and initial damage, in the exploration of progressive collapse, it is essential to distinguish between two fundamental categories: redistributional-type and impact-type collapses. These categories not only differ in their triggers but also in their underlying mechanisms and characteristics [3]. Redistributional-type collapses are the most commonly studied forms of progressive collapse [4,5]. In these scenarios, the failure of critical structural members leads to the redistribution of loads to adjacent elements. Dynamic effects due to the sudden modifications in the resisting scheme, while present, act as aggravating factors rather than a primary contributor. The focus in these cases is on identifying alternative load paths to mitigate the spread of collapse. Although significant research has been devoted to understanding redistributional progressive collapse, which occurs when loads are redistributed following the failure of key structural elements [6], much less is known about impact-type progressive collapse [7]. Impact-type collapses are fundamentally based on dynamic effects. These collapses occur when gravitational potential energy is transformed into kinetic energy, making dynamic interactions a critical component of the failure mechanism. Impact-type collapses can propagate laterally,

* Corresponding author.
E-mail address: valerio.debiagi@polito.it (V. De Biagi).

https://doi.org/10.1016/j.engfailanal.2025.109661
Received 30 January 2025; Received in revised form 13 April 2025; Accepted 28 April 2025
Available online 19 May 2025
1350-6307/© 2025 The Authors. Published by Elsevier Ltd. This is an open access article under the CC BY license (http://creativecommons.org/licenses/by/4.0/).

as domino-like effects, or along the direction of gravity, resulting in pancake-like situations [1]. It is worth noting that without these dynamic effects, impact-type collapses cannot occur.

It must be noted that speaking about collapse propagation means putting the attention on the entire structure, not on the specific element where the propagation originated. With the specific reference to the initiation of the collapse under impact conditions, two completely different approaches can be considered. In threat-dependent progressive collapse studies, the structural performance under a known impact is investigated. In this field, lots of effort has been spent in understanding the effects of impacts against structural members (say vehicle, boulders, missiles, etc.), and the consequences related to such interaction [8–10]. On the contrary, in threat-independent progressive collapse studies the impacted element is removed and the response of the structure is studied in a dynamic or quasi-static manner. Although the former approach is the most complete methodology, as the totality of the phenomenon is studied, it is also the most difficult task from a numerical and technical point of view, as the complete knowledge of the interaction between colliding body and structural member is required. Even if several scholars have tackled the problem through numerical [11–13] and experimental [14] approaches, the threat-independent methodology is definitely the most adopted, as suggested in the codes for robustness assessment [15]. However, the element removal approach must be adopted with care as it cannot lead to the worst-case scenario, in particular when catenary forces arise in the impacted member [16].

In the present paper, the attention is toward the propagation of the collapse. Among the various manifestations of progressive collapse, pancake-type collapse is a prominent example of impact-type failures. Pancake-type collapse occurs when the upper floors of a building collapse sequentially, one on top of the other, resembling the layers of a pancake [17,18]. Pancake-type collapses are the result of the evolution of damage from a single element to a more articulated mechanism involving entire floors. Although falling of debris is observed during such types of collapses, it must be clearly stated that falling debris, while a contributing factor, is generally not the true triggering event but a byproduct of the collapse itself. As observed in the failure of Plasco Building in Tehran on January 19, 2017 [19–21], such collapses can be triggered by various events, including fire, explosions, or seismic forces, that can cause the failure of multiple members. In pancake-type progressive collapse, the initial failure leads to a complete or partial loss of vertical load-bearing capacity at a certain structural level. This, in turn, initiates an impact event between the falling upper portion and the relatively intact lower portion, resulting in varying degrees of damage to the latter. Depending on the remaining capacity of the lower part, the collapse may propagate vertically, in which case a total collapse of the entire system becomes highly likely.

While experimental and numerical studies on pancake-type progressive collapse are quite limited, different aspects of the phenomenon have already been addressed in the literature. For example, punching shear failure in flat slabs, which can trigger the pancake mechanism, is discussed in [22]. A simplified analytical model for vertical building collapse triggered by the loss of all columns is presented in [17], and possible energy dissipation mechanisms are identified. Understanding the mechanisms involved in the collapse propagation is nontrivial as the final state is the result of interaction between different phenomena, starting from the triggering of the collapse, including the nonlinear behavior of elements, the second-order effects on the members, or the multi-body dynamics when the collapse progresses. The dynamic interactions that originate during such types of collapse are difficult to predict using traditional static or quasi-static models [23], leaving a critical gap in our understanding of this type of structural failure.

The collapse propagation is driven by impact interactions between structural members. Impact loading is a critical phenomenon in structural engineering that occurs when a force is applied over a short time interval, generating high-intensity stress waves and dynamic interactions between impacting and impacted bodies [24–26]. This mechanism plays a significant role in pancake-type progressive collapses, where the dynamic response of structural elements is crucial for understanding failure propagation. Initially, a localized response occurs due to the stress wave at the impact point, taking place shortly after the load application begins. Following this, the structure experiences a global response, which includes free vibration effects due to elastic and plastic deformation throughout the member over a more extended time frame [27]. These responses are influenced by factors such as the material properties of both the impactor and the target [28], as well as the rate of loading and the dynamic characteristics of the structural member [27]. Numerical simulations are essential tools for predicting the behavior of structures and contact forces during impact events [29–33]. These methods are particularly effective in capturing localized plasticity and stress distributions and often show strong agreement with experimental results for parameters such as impact duration and structural displacement. However, as noted in the study by Kishi et al. [30], numerical models may exhibit limitations in accurately predicting the maximum impact force. Researchers frequently employ finite element simulation tools, including software like LS-DYNA and Abaqus, to conduct their analyses [34–37].

Due to the complexity of the phenomenon, special attention must be paid in modeling pancake-type collapses. Finite Element approaches cannot easily catch the real failure behavior of large systems as the techniques to include element separation during modeling (namely, element erosion) are hard to control when the number of interactions increases. On the contrary, other solutions based such as Applied Element techniques [38] or hybrid methods based on physical engines [39] seem to be more affordable in predicting the final state of the system. Focusing the attention on the interaction between colliding bodies, the majority of the studies of the effects of impacts against structures deal with the concept of relative stiffness between the interacting components, classifying the impact as soft or hard [23,40,41]. In soft impacts, where the impacting body has significantly lower stiffness than the target (e.g., rubber on concrete), deformation is distributed over a larger area, and energy dissipation occurs gradually. Conversely, in hard impacts, where the impacting body has comparable or greater stiffness than the target (e.g., steel on concrete), stresses are localized, resulting in higher peak forces over shorter durations, often causing localized damage such as cracking or fracturing [42,43]. It is worth mentioning that the interaction between the impactor and the target is further governed by parameters such as contact stiffness, mass ratio, and energy dissipation mechanisms, including plastic deformation and damping [44]. When dealing with concrete structures subjected to impact loads, localized damage mechanisms, including scabbing, penetration, perforation, and

punching shear, are frequently observed [45–48]. Meanwhile, complete failure is a potential outcome and a critical concern when the magnitude of the loads increases [49–53].

With specific reference to the behavior of single members, several approaches can be adopted. The problem can be studied numerically by modeling the impacted beam subjected to a pulse load or by considering the dynamics and the interaction of the impactor in the calculations [31,54,55]. Analytical modeling involving the continuum behavior of the element has been proposed [56,57]. In alternative, multi degree-of-freedom modeling can be adopted [58]. The latter approach is suitable in beam structures, where the compliance curve of the beam can be determined with the classical structural mechanics formulations. This simplifies the study of the system as the governing equations can be easily integrated and the relevant engineering quantities can be determined. When translating a continuous beam into a lumped mass constrained with a spring and a dashpot, special attention must be paid to the value of the mass of the system, namely the so-called equivalent mass [59]. This is particularly relevant when the regime of the system changes during the phenomenon. Traditional approaches in the literature for modeling the impact response of reinforced concrete (RC) beams often consider constant factors for the equivalent mass, using values such as 0.5 [28,60] or 0.493 [61,62] for linear elastic behavior and/or 0.33 for plastic behavior [63]. Although computationally efficient, these fixed approximations fail to capture the evolving deformation profile and changes in the beam's stiffness during impact.

Focusing on the propagation of collapse due to debris falling, as the effects of impact vary significantly depending on the different scenarios, having a better understanding of which mechanisms will result in the worst conditions and under which specific conditions such propagation can occur is crucial. This study systematically addresses this gap through a parametric analysis, exploring a wide range of possible scenarios to identify the worst cases. To achieve this aim, a novel analytical model designed to simulate RC beams subjected to impact of concrete-like impactors is herein proposed. A mass–spring–damper system incorporating a variable equivalent mass, recalculated step by step based on the beam's deformation, setting it apart from traditional models with fixed mass assumptions. This approach provides a high level of accuracy in predicting contact forces and understanding energy transfer during impact events.

The reliability of the proposed model was first established through a validation study, comparing the results to experimental data. Once validated, the model was used to perform a comprehensive parametric analysis, focusing on the effects of key impact parameters such as the mass and velocity of the impactor and the geometry of the target structure. To further establish the accuracy and reliability of the proposed analytical model, a comparative analysis is performed by evaluating it against several alternative contact models. This comparison not only emphasizes the limitations of existing models in certain impact scenarios but also demonstrates how the proposed approach provides a more comprehensive and realistic representation of the beam's behavior. The reported findings provide a solid foundation for understanding impact-type collapses, particularly pancake-type scenarios observed in real-world events.

2. Contact force models

In this section, the main contact force models used to analyze impact dynamics in engineering systems are reviewed and compared. The aim is to outline the underlying assumptions, advantages, and limitations of traditional models, ranging from classical Hertzian contact theory [64] to advanced viscoelastic formulations such as the Hunt–Crossley model [44]. This overview sets the stage for introducing a novel analytical approach that incorporates a dynamically updated equivalent mass to more accurately capture the evolving deformation and stiffness changes in RC beams during impact events. In this study, we adopt the terms "reversible" and "irreversible" to describe deformations, shifting the focus from the underlying material model (elastic vs. plastic) to the observable outcomes. Reversible deformations are those that are fully recovered upon unloading, while irreversible deformations remain after the load is removed. This change in terminology better reflects the actual structural performance under impact loading.

Analytical models provide computational efficiency and offer valuable insight into contact mechanics. The Hertzian contact theory [64] forms the foundation for many such models, focusing on purely elastic deformation in the contact region. The contact force, F_c, is calculated as:

$$F_c = k_n \delta^{1.5}, \tag{1}$$

where k_n is the contact stiffness and δ is the indentation. The contact stiffness k_n for Hertzian contact is defined as:

$$k_n = \frac{4}{3} E^* R^{0.5}, \tag{2}$$

where the effective modulus of elasticity, E^*, is given by:

$$E^* = \left(\frac{1 - \nu_1^2}{E_1} + \frac{1 - \nu_2^2}{E_2} \right)^{-1}, \tag{3}$$

and the combined radius of curvature, R, is expressed as:

$$\frac{1}{R} = \frac{1}{R_1} + \frac{1}{R_2}. \tag{4}$$

Crucial to these equations are the material and geometrical properties, which determine the effective modulus of elasticity (E^*) and the contact radius (R). Here, E_1 and E_2 are the Young's moduli, and ν_1 and ν_2 are the Poisson's ratios of the impactor and impacted body, respectively. Similarly, R_1 and R_2 denote the radii of curvature of the impactor and the impacted element, respectively.

While the Hertzian model is suitable for elastic interactions, it does not account for energy dissipation or plastic deformation [65], making it idealized and less applicable for scenarios involving significant energy loss. To address these limitations, viscoelastic models such as the Kelvin–Voigt [66,67] and Hunt–Crossley [44] have been introduced. The Kelvin–Voigt model incorporates a linear spring and damper in parallel, accounting for energy dissipation through damping. The contact force in this model is represented as:

$$F_c = k_n\delta + D_n\delta\dot{\delta}, \tag{5}$$

where $\dot{\delta}$ is the indentation rate, and D_n represents the damping constant. Although this model captures energy dissipation, its linear approach makes it insufficient for non-linear contact interactions and high-velocity impacts.

For scenarios involving viscoelastic collisions, the Hunt–Crossley model builds upon the Hertzian theory by introducing a non-linear damping term to account for energy loss during impact. This model represents the contact force as [44]:

$$F_c = k_n\delta^p + D_n\delta^p\dot{\delta}, \tag{6}$$

where p is the non-linear stiffness exponent, and D_n represents the damping term, further refined by Sun et al. [68] as:

$$D_n = (0.2p + 1.3)\left(\frac{1-\mathrm{COR}}{\mathrm{COR}}\right)\left(\frac{k_n}{\dot{\delta}_0}\right). \tag{7}$$

here, the coefficient of restitution (COR) quantifies the dissipation of the collision, defined as the ratio of relative velocities after and before the impact, and $\dot{\delta}_0$ represents the initial velocity of deformation. The Hunt–Crossley model's ability to incorporate both elastic and viscoelastic behavior makes it well-suited for accounting for viscous energy dissipation [69,70]. It may not accurately capture the response of ductile materials that undergo substantial plastic deformation during impact. In such cases, the model's assumptions do not hold, and it may fail to predict the permanent deformations characteristic of ductile materials. Therefore, for materials with high ductility, alternative models that account for high plastic deformation would be more appropriate [71,72].

More sophisticated approaches, such as the Lankarani–Nikravesh model [73], extend these concepts by introducing hysteresis damping to better simulate energy dissipation. This is particularly useful for systems where the coefficient of restitution approaches unity, indicating predominantly elastic responses. These advanced models are effective in simulating rigid and flexible multibody systems and interactions involving cylindrical geometries, such as roller bearings. However, modeling such interactions often requires iterative computational techniques due to the limitations of analytical solutions for complex contact mechanics. In recent years, researchers have increasingly focused on refining and developing impact models that address various aspects of the phenomenon. For instance, Wang et al. [74] have proposed a novel elastoplastic impact model for a sphere colliding with a large plate, which incorporates energy loss from plastic deformation at the contact point as well as the dissipation of flexural waves across the plate. Sanchez et al. [75] have introduced an impact formulation for collisions between spherical rigid bodies within the framework of nonsmooth contact dynamics, taking friction effects into account.

The contact force is also highly sensitive to the test setup and experimental design. For example, the contact forces recorded by a load cell in drop-weight tests can vary significantly depending on the testing system, whether the load cell is placed directly on the specimen [76–78] or embedded within the projectile [79,80]. Some studies emphasize the need to integrate plasticity and equivalent mass concepts for accurate predictions of impact behavior [58,81]. Selecting an appropriate contact-force model is vital for accurately predicting structural responses, as the choice directly influences the representation of energy dissipation, stress distribution, and stability.

3. Methodology

This study investigates the behavior of RC beams under impact loading scenarios. The structural response of the beams is primarily governed by flexural behavior, as this study focuses exclusively on flexural failure mechanisms, neglecting shear failure and other local effects as similarly assumed in [27,82]. The RC beams considered in this analysis can experience both reversible and irreversible deformations, depending on the severity of the impact loading. A two-degrees-of-freedom (2-DOF) system was formulated to model the interaction between the impacting body and the RC beam, simulating the response of the target beam under varying impact conditions. Given the need to capture both elastic and viscoelastic behavior, along with energy dissipation during impacts, this study employs the Hunt–Crossley contact model.

3.1. Model setup

A simply supported RC beam with a span of 4 meters under the impact of a falling spherical mass with a given radius R and initial velocity v_0 was taken as the reference study case. The geometrical, material, and contact parameters of the reference beam and the impactor are summarized in Table 1. This reference scenario provides a baseline for understanding the system's dynamic behavior, which will be further compared to variations in the parametric study.

The analytical model simplifies this scenario to provide fundamental insight into the interaction between the impacting mass and the RC beam. Specifically, the beam's response is modeled using a 2-DOF system, which captures the dynamics of the impact interaction while retaining key aspects of the physical behavior. The contact parameters (COR, k_n, and p, as defined in Section 2) are based on the Hunt–Crossley framework, with their specific formulations and numerical values derived using the methodology outlined in Majeed et al. [83]. This ensures that both elastic and viscoelastic interactions are accurately represented in the model.

Table 1
Details of the reference beam and impactor.

Category	Parameter	Value
Beam geometry	Length (L)	4 m
	Width (b)	0.3 m
	Height (h)	0.45 m
	Beam total mass (m)	1350 kg
Material properties	Density (ρ)	2500 kg/m^3
	Elastic modulus (E_c)	30 GPa
	Poisson's ratio (ν)	0.2
Moment-Curvature data	Yield curvature (χ_y)	1.2×10^{-2} rad/m
	Yield moment (M_y)	119 kNm
	Ultimate curvature (χ_u)	5.77×10^{-2} rad/m
	Ultimate moment (M_u)	126 kNm
Impactor properties	Mass of the impacting body (m_i)	100 kg
	Initial velocity (v_0)	6 m/s
Contact properties	Contact radius (R)	0.423 m
	Coefficient of restitution (COR)	$-0.0043 \cdot v_0 + 0.1919$
	Contact Stiffness (k_n)	$236709 \cdot v_0 + 2 \times 10^6$ N/m
	Exponent of Hunt–Crossley model (p)	$0.0209 \cdot v_0 + 0.8579$

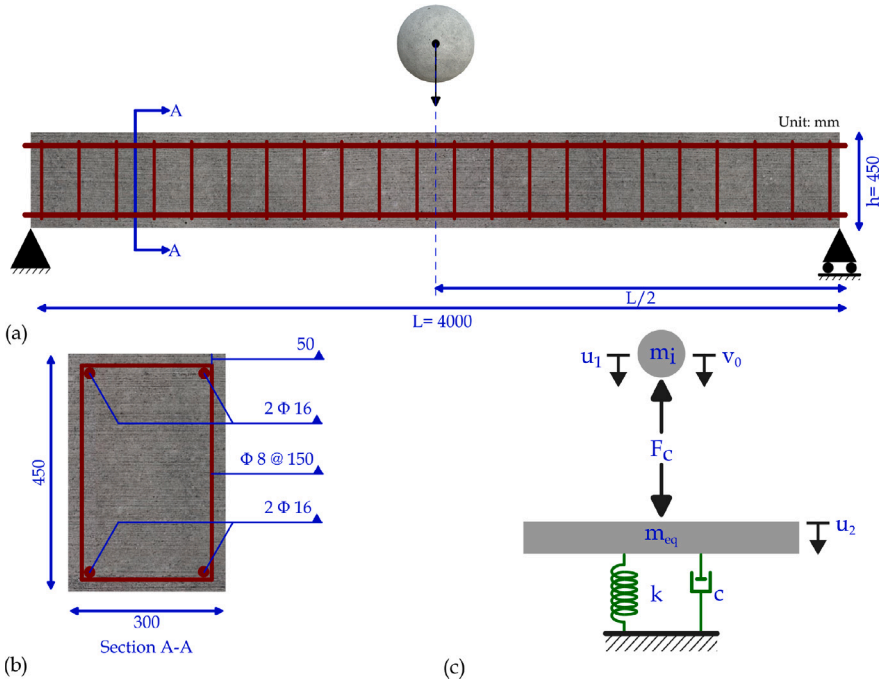

Fig. 1. Impact of a spherical mass on a simply supported RC beam at midspan: (a) overall configuration, (b) cross section of the impacted beam, and (c) equivalent 2-DOF impact model showing the dynamic interaction between the impactor and the beam.

Fig. 1 illustrates the setup of the reference case, including both the real-world impact scenario and its analytical equivalent. Fig. 1(a) illustrates the impact of a spherical mass on a simply supported RC beam with a specified span length and a midspan impact point. Fig. 1(b) shows the cross-sectional view of the impacted beam, which is identical for all samples in this study. Fig. 1(c) presents the analytical equivalent 2-DOF system. It consists of two components. The impacting body is modeled as a point mass of value m_i, whose position and velocity are described through variables u_1 and $\dot{u_1}$, with the dot representing the derivative with respect to time. As the impacting mass is considered as a rigid body, u_1 both defines the position of the centroid of the mass and also the position of the bottom point of the impacting sphere, i.e., the contact point in the real impact.

The impacted beam is modeled as a body connected to a fixed reference system with a spring and a dashpot. The position of the mass, namely u_2, reflects the position of the midspan point of the beam. The stiffness k of the connecting spring represents the tangent vertical stiffness of the beam midpoint for a given value of a vertical force acting at midspan. The mass of the impacted body is denoted as m_{eq}, and it is the equivalent mass, which depends on the deformed shape of the beam, as detailed in the following. The

impacting mass and the impacted body interact with each other thanks to the contact force F_c, which depends on the indentation, $\delta = u_1 - u_2$, and on the indentation velocity, $\dot{\delta} = \dot{u}_1 - \dot{u}_2$.

The governing equations of motion for the system are:

$$\begin{cases} m_i \ddot{u_1} + F_c(u_1, u_2, \dot{u_1}, \dot{u_2}) = m_i g, & (8) \\ m_{eq} \ddot{u_2} + c\dot{u_2} + k u_2 = F_c(u_1, u_2, \dot{u_1}, \dot{u_2}), & (9) \end{cases}$$

where Eq. (8) describes the dynamic equilibrium of the impacting mass, while Eq. (9) is the dynamic equilibrium of the impacted element. Gravity g was introduced into the impacting mass only, as the dead load displacements of the beam are neglected.

The governing equations of motion were implemented in MATLAB [84] and solved using the ODE113 solver, a variable-step solver well-suited for handling stiff differential equations. The time span for the simulation was set to 0.1 s, with a maximum time step size of 0.01 ms to ensure numerical stability and precise resolution of the dynamic response. The beam's compliance curve was pre-calculated to dynamically update the equivalent mass and stiffness during the simulation. Initial conditions included zero displacement for the target beam and a velocity derived from the impactor's free-fall height. At each step, the compliance curve was interpolated to capture transitions between elastic and plastic behavior, incorporating plastic deformation and residual displacements. Unlike traditional models that assume a constant equivalent mass [28], this approach dynamically recalculates m_{eq} throughout the interaction process, ensuring the beam's dynamic behavior is accurately captured as it transitions between elastic and plastic deformation.

3.2. Equivalent mass calculation

The calculation and continuous update of the equivalent mass (m_{eq}) and stiffness (k) are the cornerstones of this study. This approach introduces two key novelties: the equivalent mass and stiffness are calculated step by step based on the evolving deformation of the beam during the simulation, and the model accounts for unloading paths and residual displacements, ensuring that the system can reflect realistic structural behavior, including irreversible deformation and energy dissipation.

The methodology for computing m_{eq} consists of two primary steps.

3.2.1. Step 1: Pre-calculating the compliance curve

The equivalent mass and stiffness are derived from a pre-calculated compliance curve of the beam, which characterizes the beam's force–displacement behavior under mid-span loading. The compliance curve is generated by incrementally applying a control force at the beam's mid-span and computing the corresponding displacement. This process accounts for material nonlinearity by considering the moment–curvature relationship of the beam. As the applied force increases, the beam undergoes increasing curvature, initially following an elastic response. However, once the bending moment exceeds the yield moment M_y, the curvature grows nonlinearly, indicating plastic deformation. The compliance curve captures this transition by mapping the displacement to the corresponding force, reflecting the nonlinear force–deformation relationship and the progressive reduction in stiffness as the beam enters the plastic regime.

To compute the compliance curve, given a value of the force at midspan, the bending moment of the beam is computed. Based on the moment–curvature relation, the curvature diagram is obtained. The double integration of the curvature, along with the imposed boundary conditions (null vertical displacements at the ends), provides the displacement $W(x)$ of the beam. The compliance curve is the force-midspan relationship.

This compliance curve, determined based on the geometry and material properties of the beam, remains fixed throughout the simulation and serves as the reference for determining the beam's behavior at any given displacement or force level. Importantly, the compliance curve also accounts for non-linear behavior, capturing transitions between elastic and plastic states, as the moment–curvature relation of the cross-section is adopted.

3.2.2. Step 2: Dynamic recalculation during simulation

During the impact simulation, the pre-calculated compliance curve is used to dynamically update the equivalent mass (m_{eq}) and stiffness (k) at each time step. This is achieved through the following process. First, (i), at each time step, the displacement of the beam (u_2) is computed as part of solving the governing equations of motion, Eq. (9). Then (ii), the pre-calculated compliance curve is interpolated to determine the corresponding force at u_2, which accounts for material nonlinearity through the moment–curvature relationship. (iii) The equivalent mass is recalculated based on the deformed shape of the beam. Using the deflection profile:

$$\Phi(x) = \frac{W(x)}{W(u_2)}, \quad (10)$$

the equivalent mass is computed as:

$$m_{eq} = \frac{m}{L} \int_0^L \Phi^2(x)\, dx, \quad (11)$$

this ensures that regions with greater deflection contribute more to the beam's dynamic response; Finally, (iv) the compliance curve is updated dynamically to reflect any material plasticity. If the system enters the plastic regime, the compliance curve shifts to account for permanent deformations, modifying both the stiffness and the equivalent mass for subsequent time steps.

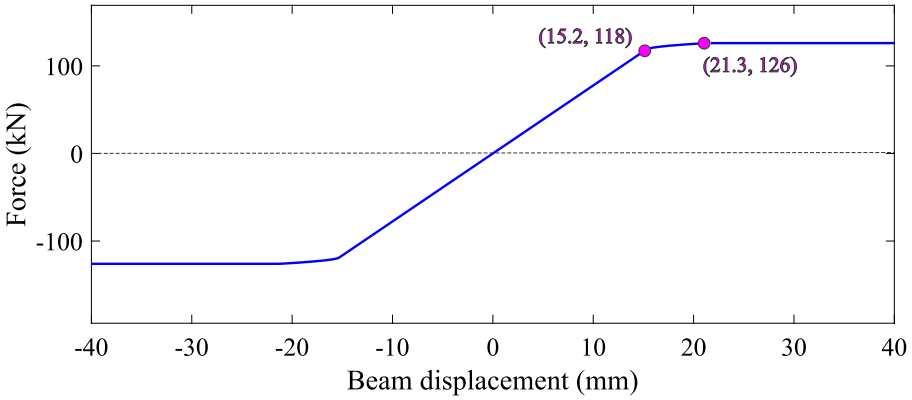

Fig. 2. Compliance curve of the reference beam.

This iterative approach enables a real-time adjustment of the beam's dynamic properties, ensuring accurate simulation of its evolving stiffness and mass distribution under impact loading.

If the system undergoes unloading, the compliance curve adjusts step by step to follow the correct unloading path, ensuring consistency with the nonlinear behavior of the material. Fig. 2 illustrates the pre-calculated compliance curve, which serves as a central reference for dynamic updates throughout the simulation. From the compliance curve (Fig. 2), it can be seen that the reference beam, as described in Section 3.1, yields at a displacement around 15.2 mm. In addition, there is a second bend in the compliance curve, marking 21.3 mm as a critical point. These two points represent key transitions in the beam's behavior under impact loading, with the 15.2 mm point indicating the onset of yielding and the 21.3 mm point indicating further progression toward ultimate displacement, i.e. when the plastic hinge is fully developed.

To benchmark the proposed approach, a comparison was made with the hybrid model proposed by Yong [28]. In that model, a fixed equivalent mass factor was used for calculating the maximum contact force, incorporating a correction factor into the non-linear elastic model to align its predictions with those of the Hunt–Crossley model. The results of this comparison are available in Section 4.

3.3. Validation of the model

The validation of the proposed analytical model was conducted using the experimental results reported by Fujikake et al. [27], which provide a comprehensive assessment of the impact response of RC beams. The beam S1616 was simply supported over a span of 1.4 m and had cross-sectional dimensions of 250 mm in depth and 150 mm in width. The beam was reinforced with D16 bars as longitudinal reinforcement on both the compression and tension sides. Stirrups of D10 bars were spaced at 75 mm. A hammer with a mass of 400 kg and a hemispherical tip with a radius of 90 mm was released to freely impact the midspan of the beam at the top surface from a height of 1.2 m. Fig. 3 illustrates the specimen details and the experimental test setup [27]. The validation process involved simulating the test scenario in MATLAB using the proposed analytical model. Key outputs, such as contact forces and midspan deflections, were compared with experimental data from Fujikake et al. [27] to evaluate the model's accuracy.

Fig. 4 presents the measured impact loads and midspan deflections recorded during the laboratory test, alongside the predictions from the proposed analytical model. Comparisons between the experimental results and the predictions made in the current work demonstrated a maximum displacement difference of less than 2%, confirming the accuracy and reliability of the developed model. Determining the source of discrepancies between experimental and analytical results can be challenging, particularly in cases of extreme loading scenarios or when the difference is negligible. In general, two categories of potential sources can be considered. The first pertains to general factors that typically affect comparisons and are inherently difficult to account for. Most notably, experimental models often exhibit slight imperfections in material properties and geometry, which may influence the results. Moreover, the idealized boundary conditions commonly assumed in analytical and numerical studies cannot fully capture the potential for near hinged support behavior or minor slips. The second category relates to the assumptions and simplifications adopted in the present study. For instance, as in many analytical and numerical studies, a perfect bond between steel and concrete is assumed. However, in a reinforced concrete beam under impact, micro-slips or partial debonding may occur. Additionally, the material model used in this study is elastic–plastic, and strain rate effects as well as post-peak damage are not considered. Furthermore, the developed model does not account for potential local damage at the surface and sub-surface level that may occur in a real scenario considering the effects on the underlying layers in composite materials. In an experimental setting, these factors can partially influence the response. Given the slight discrepancy between the experimental and analytical models, identifying the primary source of error is challenging. However, the overall agreement in both the maximum value and general trend underscores the model's ability to predict dynamic responses under impact loading with a high degree of accuracy, demonstrating that the developed model effectively serves the main objectives of the study.

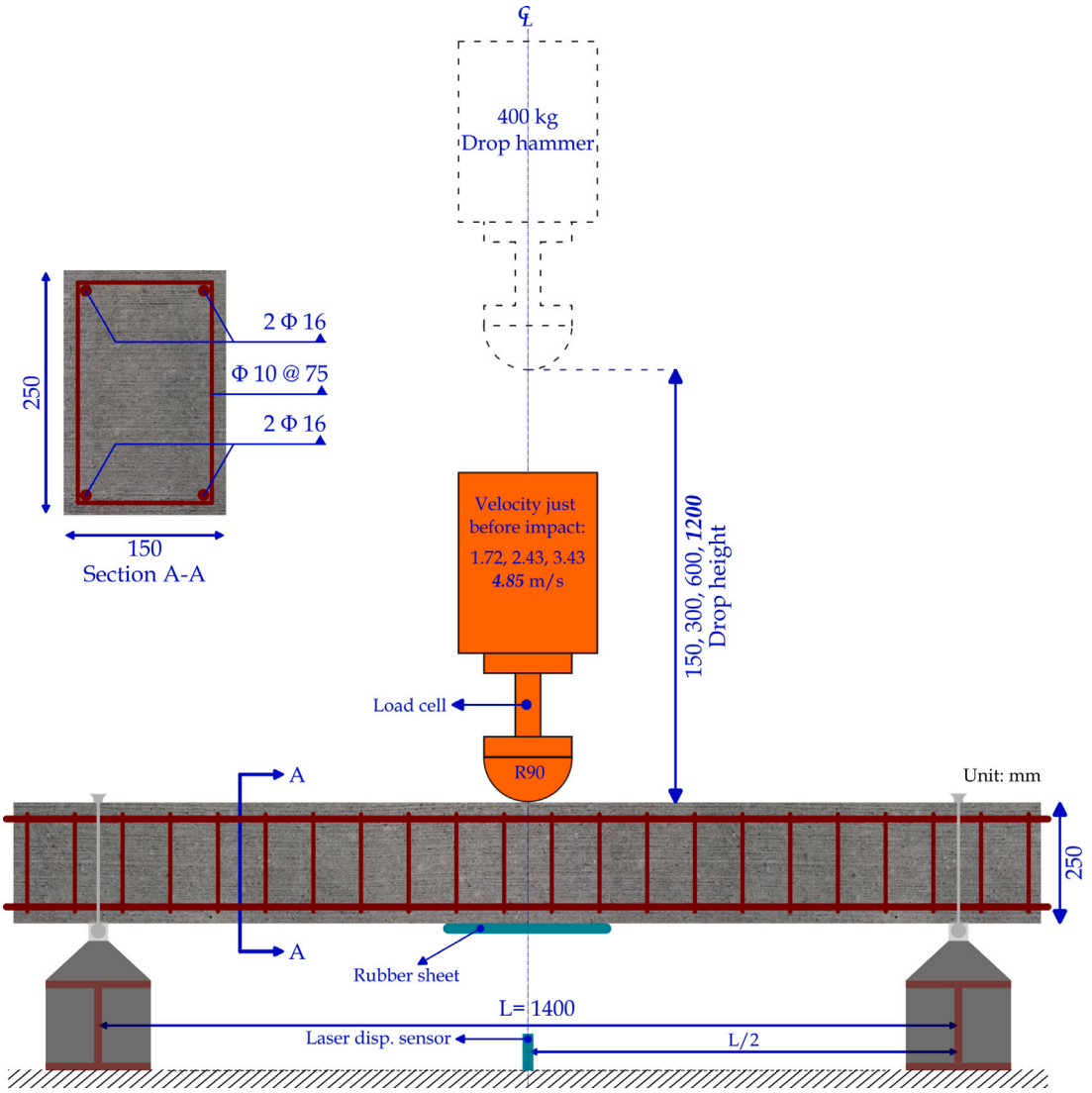

Fig. 3. Drop hammer impact test setup, rebar arrangement and cross-sectional view of Fujikake's study [27].

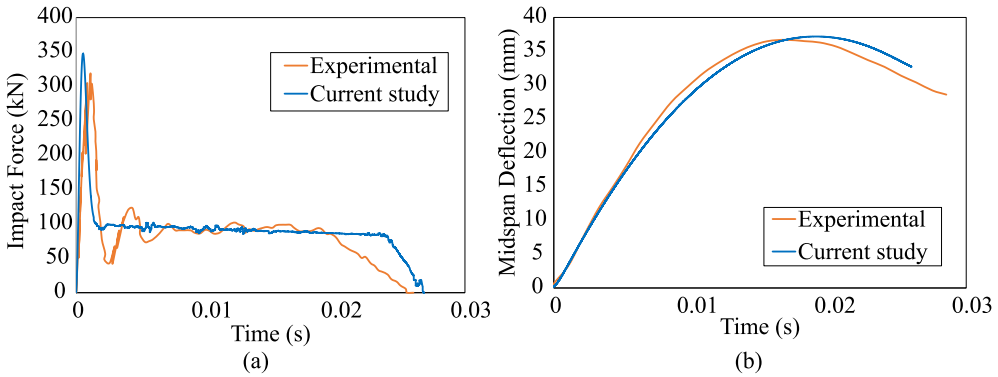

Fig. 4. Comparison of experimental impact response results for specimen S1616 from Fujikake's study [27] with predictions from the current study: (a) impact force vs. time, and (b) midspan deflection vs. time.

Table 2
Parametric study variables and their ranges.

Parameter	Range
Mass of the impacting body (m_i)	50 kg to 500 kg
Initial velocity of the impactor (v_0)	2.5 m/s to 30 m/s
Beam Length (L)	2 m to 6 m

3.4. Parametric study

The primary parameters investigated in this study, along with their respective ranges, are summarized in Table 2. These parameters were chosen because they represent fundamental aspects of the impact event, including the properties of the impacting body, the beam geometry, and the initial impact conditions. For each simulation, one parameter was varied while the others were kept constant at the reference values detailed in Table 1, ensuring a controlled assessment of each variable's influence. Impact kinetic energies in the range 0.156 kJ to 225 kJ were investigated.

Since this study involves a parametric analysis, there is no specific emphasis on selecting the most realistic scenarios for the parameter ranges. However, these ranges are reasonable for typical RC structures subjected to common impact scenarios that may occur during extreme events. In many cases, the ranges were intentionally extended to encompass the most possible cases, providing a comprehensive understanding of structural behavior under a wide spectrum of extreme loading conditions.

As mentioned before, the simulations were performed using MATLAB's ordinary differential equation (ODE) solver (ODE113). Initial conditions included zero displacement for the RC beam, a pre-calculated compliance curve reflecting the beam's geometry and material properties, and an impact velocity derived from the specified v_0. Key outputs, such as the contact force (F_c) and midspan displacement (u_2), were analyzed to identify trends and insights into the beam's response under varying impact scenarios.

A comparative study is conducted with two established methods: the classical Hertzian contact model and the approach proposed by Yong [28]. Both the current study and Yong's method utilize the Hunt–Crossley contact model; however, the key difference lies in the treatment of mass and stiffness. For a simply supported beam with a span length of 4 m, the current model recalculates the equivalent mass and stiffness step by step based on the evolving deformation of the beam, whereas Yong's approach employs fixed values. Two sets of impact scenarios are considered: one set involves impactor masses ranging from 50 kg to 500 kg at a constant initial velocity of 6 m/s, and the other set uses a fixed impactor mass of 100 kg with the initial velocity varying from 2.5 m/s to 25 m/s. The findings of the parametric study and the comparative analyses are shown and discussed in detail in Sections 4 and 5.

4. Results

This section presents the results from the parametric study, focusing on the dynamic response of the RC beam subjected to various impact conditions. The analysis covers the effects of varying impactor mass, initial velocity, and beam length on key parameters such as contact force, displacement, velocity, and indentation. To further validate the accuracy and reliability of the proposed analytical model, a comparative study is conducted between the Hertzian contact model, the Yong method [28], and the current study.

4.1. Discussion on the behavior of the reference case

Regarding the analysis of the reference case, where the impactor has a mass of 100 kg, an initial velocity of 6 m/s, and the beam has a span length of 4 m, several key observations can be made. All results presented (e.g., velocity-displacement loops, force-indentation curves, and deflection time-histories) are based solely on the contact phase, during which the impactor interacts with the beam. Figs. 5 and 6 present various aspects of the beam's dynamic response during impact and provide a schematic representation of the reference case.

Fig. 5(a) illustrates the displacement-time response of both the impactor and the beam. The difference between these two curves represents the indentation δ, which characterizes the localized deformation at the impact interface. Initially, the indentation starts from zero and progressively increases, reaching its maximum value within the first 2 ms of contact. Subsequently, the indentation starts decreasing as the impactor begins to rebound. When the contact phase concludes, the indentation returns to zero. The total contact duration is 35.25 ms (ms), indicating the complete interaction between the impactor and the beam before separation.

Fig. 5(b) presents the indentation and indentation velocity as functions of time. The indentation velocity is maximum at the first instants of the contact, when the interaction starts. It is interesting to note that the interaction velocity has a peak in the very first instants of the contact. This is relevant, as discussed further, as the indentation velocity has an effect on the collision force.

As the indentation increases, the velocity gradually decreases. Around the moment of maximum indentation, the indentation velocity shifts from positive to negative values, indicating the reversal of motion and the onset of unloading. This phase transition highlights the influence of energy transfer between the impactor and the beam, where the beam absorbs kinetic energy and subsequently releases it during unloading.

Fig. 6(a) shows the evolution of contact force over time. The plot included in the figure focuses on the first 2 ms of contact duration, when the force peaks. After 2 ms, the contact force remains nearly negligible until it fully dissipates at 35 ms. The focus on the first 2 ms in Fig. 6(a) is to highlight the active phase where the force rapidly increases and decreases, while the later period involves minimal force as the system progresses toward complete unloading. The peak contact force of 858 kN occurs

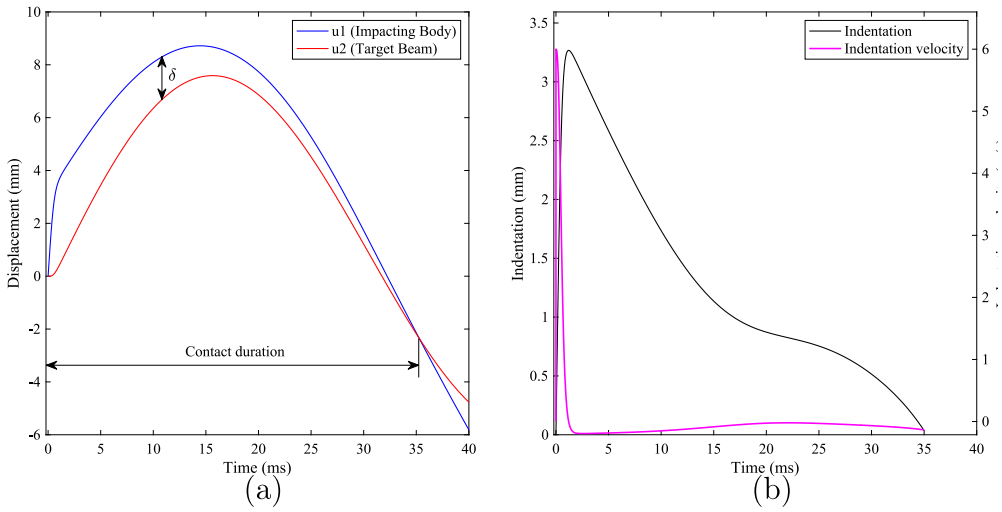

Fig. 5. Analytical results of reference case: (a) displacement of the impactor and the impacted beam over time, and (b) indentation and indentation velocity during contact.

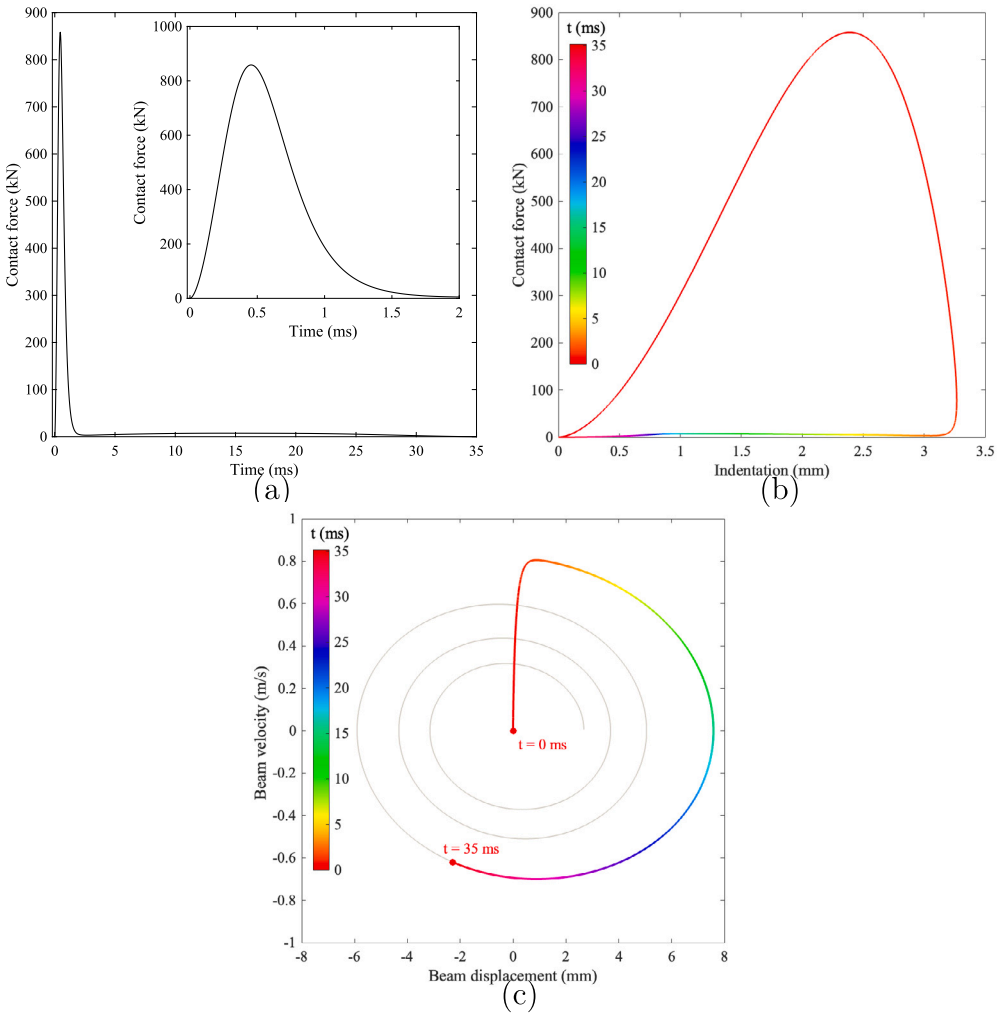

Fig. 6. Analytical results of reference case: (a) contact force vs time, (b) contact force vs indentation, (c) beam velocity vs beam displacement during contact.

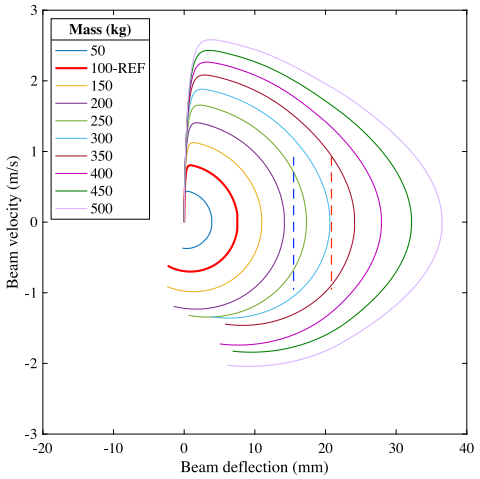

Fig. 7. Beam velocity-beam displacement under different impactor masses. The blue and red vertical dashed lines at 15.2 mm and 21.3 mm represent the yield and critical displacement points from the compliance curve, respectively.

at approximately 0.45 ms, at which point the beam's displacement is only 1 mm. After reaching its maximum, the contact force gradually decreases, while the beam displacement continues to increase. The maximum beam displacement of approximately 7.6 mm occurs around 15 ms after the impact begins.

Fig. 6(b) provides key insights into the loading and unloading behavior through the force-indentation curve. The temporal information is reported in the plot as the color of the line is related to the time. As evident from the plot, the unloading phase begins while the indentation is still increasing. This continues until the indentation reaches its maximum value of 3.2 mm, at which point the contact force is approximately 100 kN. Even during unloading, the indentation gradually reduces from 3.2 mm to zero, returning to its initial state as the contact force approaches zero. It is interesting to note that the peak of the curve occurs when the indentation velocity is close to its maximum. Analyzing the contributions of Eq. (6) in the collision force-indentation plot, it results that the Hertzian part, representing the first term of Eq. (6) provides a limited contribution to the overall force, while the larger contribution is associated to the damping term, i.e. the second addend of Eq. (6).

Fig. 6(c) represents the evolution of beam velocity with displacement, providing a comprehensive view of the beam's dynamic oscillations. The complete curve, in gray, refers to the behavior of the beam in the first 180 ms. The gray curve is overlapped with a detail of the contact phase of the interaction, represented with a colored line that reflects the evolution with time. At the beginning of the impact, when the beam displacement is merely 1 mm, the beam velocity reaches its maximum value of 0.8 m/s. As the beam continues to displace, the velocity progressively decreases, reaching zero at the maximum displacement of 7.6 mm. This marks the transition point where the beam reverses its motion. As the beam moves back toward its original position, it gains velocity in the opposite direction. Notably, when the velocity reaches its maximum negative value, the beam displacement is still 0.87 mm. The curve shows two phases of interaction. The colored segment from 0 to 35 ms, with the time gradient shown in the legend, refers to the collision phase, indicating contact occurrence, i.e., when the indentation is greater than zero. The gray segment refers to the free vibration of the beam. In the following, all the curves are plotted only for the collision phase.

4.2. Effect of varying impactor mass

The impactor mass is a critical variable in determining the dynamic response of the RC beam. The simulation results highlight how changes in impactor mass significantly influence key parameters such as contact force, displacement, and indentation, with higher mass impactors inducing greater deformations and more pronounced plastic behavior. Figs. 7 and 8 report the effects of varying impactor mass.

For impactor masses ranging from 50 to 200 kg, the loops in Fig. 7 remain mostly to the left of the 15.2 mm line, suggesting the beam stays within or near the elastic range. The unloading paths of the force-indentation curves (Fig. 8.a) show limited deviation from the loading paths, indicating predominantly reversible behavior with minimal residual deformation. By comparing Table 3 with the compliance curve (Fig. 8.b), it is observed that the maximum displacement in this case remains below 15.2 mm, confirming negligible irreversible deformation.

For impactor masses ranging from 250 to 300 kg, the beam begins to enter the plastic region. The maximum displacements for m_i = 250 kg and m_i = 300 kg are 17.3 mm and 20.6 mm, respectively (Table 3), which fall between the yielding (15.2 mm) and critical points (21.3 mm) of the compliance curve. In Fig. 7, the loops expand horizontally (reflecting increased beam deflections) and vertically (showing higher velocity magnitudes). Force-indentation curves (Fig. 8.a) for these masses show more distinct curves and a larger enclosed hysteresis area, with the unloading paths deviating from the loading paths, indicating permanent deformation and increased energy absorption. The deflection-time curves (Fig. 8.b) show that the time at which the maximum deflection occurs

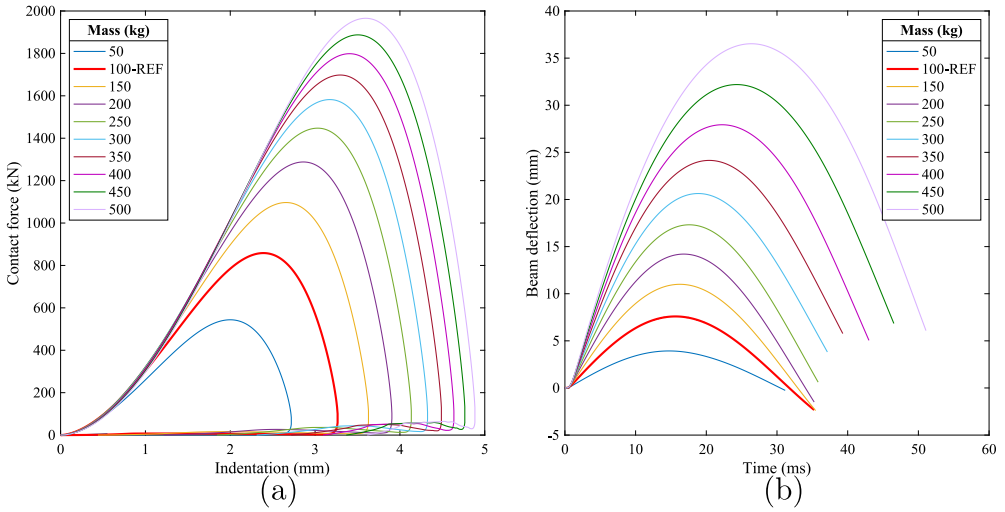

Fig. 8. (a) Contact force-indentation and (b) beam deflection time-history based on different impactor masses.

Table 3
Summary of beam impact analysis for various masses.

Impactor	Contact force		Displacement		Contact
mass (kg)	Max force (kN)	Time at max force (ms)	Max disp (mm)	Time at max disp (ms)	duration (ms)
50	544	0.38	3.9	14.7	31.16
100	858	0.45	7.6	15.6	35.26
150	1096	0.50	11	16.3	35.46
200	1288	0.54	14.2	16.8	35.26
250	1447	0.58	17.3	17.5	35.82
300	1582	0.60	20.6	18.9	37.13
350	1698	0.62	24.1	20.3	39.31
400	1799	0.64	27.9	22.1	43.01
450	1965	0.67	31.9	24.3	46.53
500	2147	0.68	36.5	26.2	51.08

increases as the impactor mass increases. For impactors with lower mass, the beam reaches its peak displacement faster (e.g., 14 ms for the impactor mass of 50 kg), while for impactors with more mass, it takes longer (26 ms for 500 kg).

For impactor masses ranging from 350 to 500 kg, the maximum displacement exceeds 21.3 mm, indicating that the beam has reached its fully plastic regime. For m_i = 500 kg, the maximum displacement reaches 36.5 mm (Table 3). The force-indentation curves (Fig. 8.a) show pronounced loops, with large areas between loading and unloading paths, highlighting energy absorbed and dissipated due to viscous phenomena at the contact interface. The duration of the contact, reported in the last column of Table 3, or identified as the end points of the time-histories of the displacement of the beam plotted in Fig. 8.b, increases with the mass.

A comparative analysis of the reference case (m_i = 100 kg) and the heaviest case (m_i = 500 kg) reveals the following trends. Increasing the mass from 100 kg to 500 kg (a factor of 5) results in nearly a 5-fold increase in maximum displacement, from 7.6 mm to 36.5 mm (Table 3). The maximum contact force increases from 858 kN to 2147 kN (a factor of 2.5), indicating that while both displacement and contact force increase with impactor mass, the beam's displacement response is proportionally more sensitive to changes in mass. The area in Fig. 8.a increases substantially, reflecting greater energy absorption and dissipation through irreversible deformation as the mass increases.

Table 3 shows that the total contact duration increases noticeably with impactor mass, ranging from approximately 31 ms for the 50 kg impactor to over 51 ms for the 500 kg impactor. This longer contact period for higher masses implies that the beam remains under significant load for a greater length of time, facilitating more pronounced deformation. Additionally, the time at which maximum displacement occurs also grows with mass, suggesting that impactors with higher masses induce a slower buildup of deformation due to both inertial effects and the onset of plastic behavior. Consequently, while lower-mass impacts exhibit shorter, more elastic interactions, higher-mass impacts produce extended contact durations that lead to greater energy transfer and more sustained beam motion.

By multiplying the mass by 5 – from 100 kg to 500 kg – the initial kinetic energy increases fivefold (from 1.8 kJ to 9 kJ, respectively), and accordingly, the restitution coefficient (COR) is almost 2 times lower (from 0.0527 to 0.0263), which correlates with roughly 3.3 times larger energy loss (from 1.547 kJ to 5.092 kJ), as evidenced by the area enclosed in the force-indentation loop (Fig. 8.a). These observations are in line with the findings reported in [85].

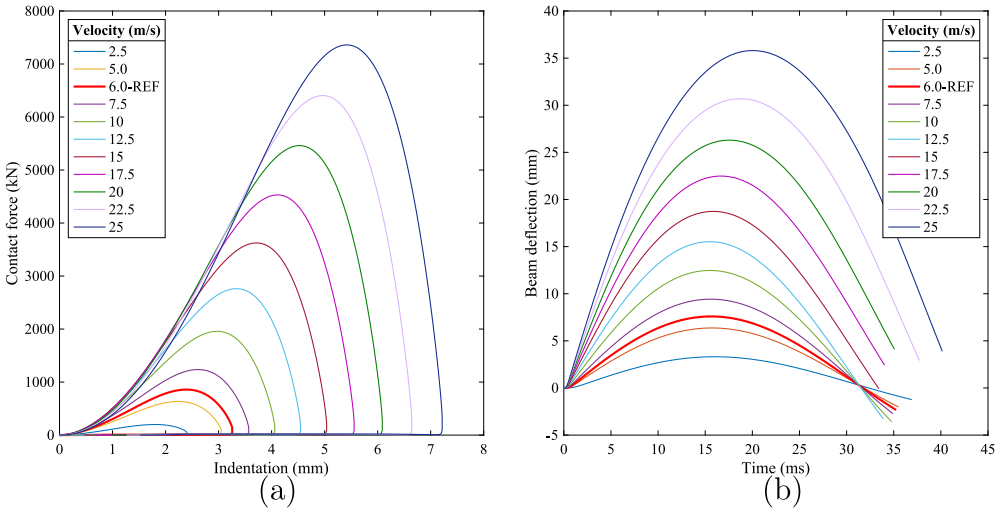

Fig. 9. (a) Contact force-indentation and (b) beam deflection time–history for different impactor initial velocities.

4.3. Effect of varying impactor initial velocity

The influence of the impactor initial velocity on the beam's dynamic response was examined through several key parameters. In Fig. 9.a, the contact force-indentation plots reveal that higher velocities result in steeper initial force increases, reflecting the beam's immediate resistance to deformation. For instance, at an indentation of approximately 1.5 mm, the contact force for a low velocity of 5 m/s is around 500 kN, whereas for a high velocity of 25 m/s (a fivefold increase), it exceeds 1500 kN, showing a threefold increase. Similarly, the maximum contact force increases from approximately 800 kN at 5 m/s to over 7300 kN at 25 m/s, demonstrating a disproportionate response to higher velocities.

Comparing the cases with an initial velocity of 5 m/s and 25 m/s shows that, for a fixed mass, the initial kinetic energy increases from 1.25 kJ to 31.25 kJ (a 25-fold increase), while the restitution coefficient (COR) decreases from 0.0617 to 0.0153 (roughly 4 times lower). Consequently, the energy dissipated in the force–indentation loop rises from 1.1 kJ to 27 kJ (approximately 24.5 times higher). These findings are consistent with continuous contact models, as reported in [85],

The deflection time-histories in Fig. 9.b further confirm these observations. Low-velocity impacts (5 m/s) lead to small, recoverable deflections of around 7 mm, whereas higher velocities (25 m/s) induce larger, permanent deflections of up to 35 mm. This indicates a fivefold increase in maximum deflection for the same increase in velocity. Additionally, the duration of maximum deflection increases from around 15 ms at 5 m/s to beyond 20 ms at 25 m/s, highlighting the prolonged influence of dynamic effects under higher kinetic energy inputs. It is worth noting that the duration of the contact, represented by the end points of the time–history curves in Fig. 9.b, has a double trend: starting from 36.91 ms for a 2.5 m/s impact it reduces to 33.90 ms for a 12.5 m/s impact velocity. For larger velocities, the figure starts increasing: at 25 m/s the contact duration is 40.15 ms.

Lastly, Fig. 10 presents beam velocity-deflection loops, which expand significantly with velocity. The transition between the elastic and the plastic stage of the beam occurs at an impact velocity of 12.5 m/s, as the curve corresponding to such velocity is almost tangent to the dashed vertical blue line representing the yield displacement at 15.2 mm. It is worth mentioning that 12.5 m/s corresponds to the transition observed for the contact duration previously highlighted. The loops' widening with increased velocity reflects not only higher energy absorption but also greater irreversible deformation, with deflections reaching up to 35 mm. This demonstrates that higher initial velocities induce more extensive damage within the flexural failure mode.

4.4. Effect of varying beam length

The dynamic response of RC beams under impact loading is significantly influenced by beam length, as evident from Figs. 11 and 12. A detailed comparison of beams with varying lengths reveals critical insights into their stiffness, energy absorption capacity, and deformation behavior. In Fig. 11.a, the contact force versus indentation curves show that shorter beams exhibit lower peak contact forces, while longer beams generate higher forces, despite having lower stiffness. Despite these differences in peak contact force, the overall trend of the curves remains consistent across beam lengths.

The deflection time-histories in Fig. 11.b highlight the relationship between beam length and dynamic response. At $t = 5$ ms, the deflection of the 2 m beam is 1.5 times higher than that of the 6 m beam. However, as the impact progresses, shorter beams, which are stiffer, recover more rapidly, with peak deflections of approximately 3.5 mm for the 2 m beam and 7.5 mm for the 4 m beam, and recovery times of 9 ms and 32 ms, respectively. In contrast, longer beams demonstrate significantly larger deflections, reaching up to 12 mm, with recovery times exceeding 70 ms.

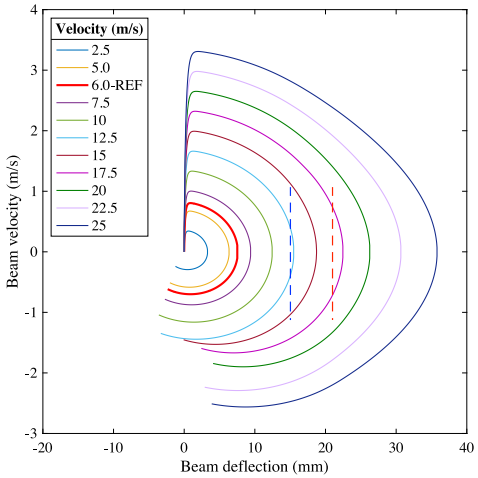

Fig. 10. Beam velocity-beam deflection resulted from different impactor initial velocity. The blue and red vertical dashed lines at 15.2 mm and 21.3 mm represent the yield and critical displacement points from the compliance curve, respectively.

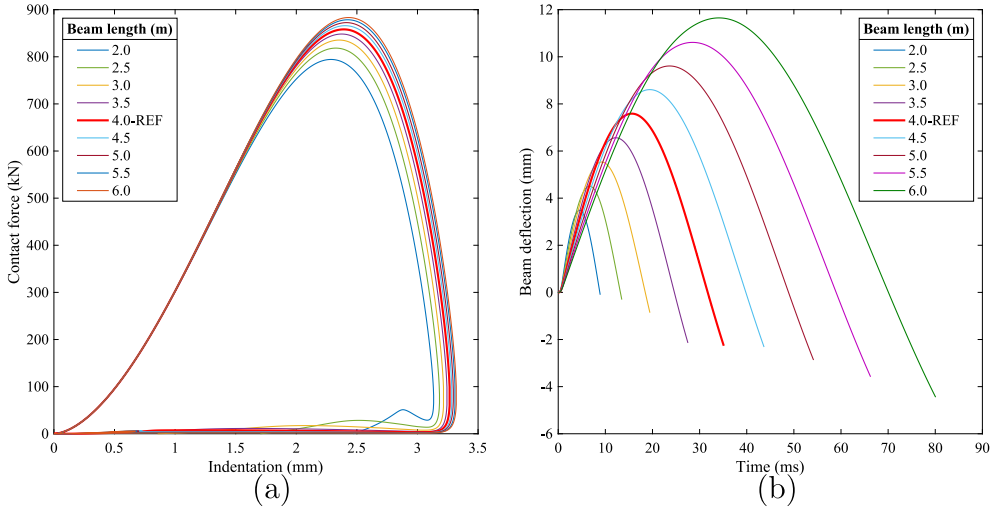

Fig. 11. (a) Contact force-indentation and (b) beam deflection time–history for different beam lengths.

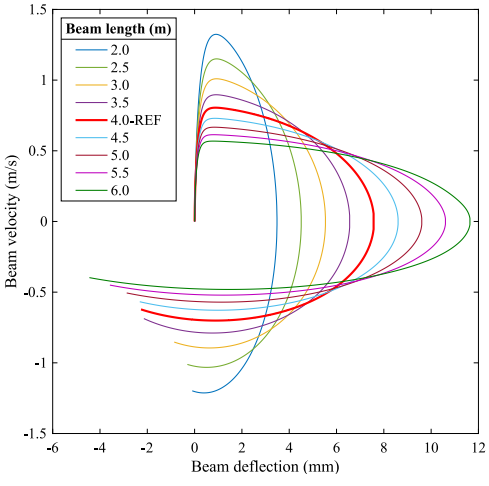

Fig. 12. Beam velocity-beam deflection resulted from different beam length.

Table 4
Comparison of max contact forces and percentage differences across methods. The labeling scheme for the samples follows the format $m_i X v_0 Y$, where X refers to the value of the impactor mass (in kilograms), and Y denotes the value of the initial velocity of the impactor (in meters per second).

Sample	Max contact force (Hertz) (kN)	Max contact force (Yong) (kN)	Max contact force (Current study) (kN)	% Diff (Hertz and Current study)	% Diff (Yong and Current study)
$m_i 50 v_0 6$	964	576	544	+43.57	+5.56
$m_i 100 v_0 6$	1530	936	858	+43.92	+8.33
$m_i 150 v_0 6$	2005	1223	1096	+45.34	+10.38
$m_i 200 v_0 6$	2429	1465	1288	+46.97	+12.08
$m_i 250 v_0 6$	2819	1674	1447	+48.67	+13.56
$m_i 300 v_0 6$	3183	1859	1582	+50.30	+14.90
$m_i 350 v_0 6$	3528	2023	1698	+51.87	+16.07
$m_i 400 v_0 6$	3856	2171	1799	+53.35	+17.13
$m_i 450 v_0 6$	4171	2306	1965	+52.89	+14.79
$m_i 500 v_0 6$	4475	2428	2147	+52.02	+11.57
$m_i 100 v_0 2.5$	535	210	199	+62.80	+5.24
$m_i 100 v_0 5.0$	1230	689	635	+48.37	+7.84
$m_i 100 v_0 7.5$	2000	1354	1236	+38.20	+8.71
$m_i 100 v_0 10$	2825	2151	1957	+30.73	+9.02
$m_i 100 v_0 12.5$	3692	3042	2762	+25.19	+9.20
$m_i 100 v_0 15$	4595	3996	3624	+21.13	+9.31
$m_i 100 v_0 17.5$	5529	4994	4531	+18.05	+9.27
$m_i 100 v_0 20$	6490	6017	5460	+15.87	+9.26
$m_i 100 v_0 22.5$	7475	7053	6404	+14.33	+9.20
$m_i 100 v_0 25$	8482	8094	7360	+13.23	+9.07

4.5. Comparison between contact models

Referring to the maximum interaction force, the maximum contact force for the Hertzian model can be obtained by integrating the force indentation curve up to the point in which the strain energy equals the kinetic energy of the impacting mass. It results that the maximum force for an Hertzian contact model is [28]:

$$F_{Hz,max} \approx \frac{3}{4} E^* \sqrt{R} \left(\frac{m_i v_0^2}{E^* \sqrt{R}} \right)^{3/5}. \tag{12}$$

Yong et al. [28] have implemented a closed form expression of the maximum collision force of a mass over a plane in which the interaction follows the Hunt–Crossley model: the formula is reported as Eqn. (6.32) in [28] and has been analytically found by taking into account the elliptical relationship between indentation and its rate (the cited document reports the complete mathematical derivation). Both previous formulations do not take into account the fact that the impacted body can deform. In this subsection, a comparison of the results obtained from three different methods, i.e. Hertzian, Hunt–Crossley with Yong's approach [28], and the current study, is presented. Table 4 summarizes the maximum contact forces calculated using these methods for varying impactor masses and velocities, along with the percentage differences between them.

For impactor masses ranging from 50 kg to 500 kg, the differences between the Hertzian model and the current study remain consistently around 50%. In contrast, Yong's approach shows smaller deviations from the current study for lower mass and lower velocity cases (e.g., masses $\leq$ 200 kg and velocities $\leq$ 10 m/s).

5. Discussions

For the reference case (impactor mass equal to 100 kg, initial velocity equal to 6 m/s, and beam span of 4 m), the results indicate a delayed peak displacement (15.15 ms) relative to the peak contact force. This delayed response demonstrates the significant role of inertia resistance, where the beam resists immediate deformation and undergoes progressive displacement as the applied force dissipates. The presence of a loop in the force–indentation response further confirms that a fraction of the impact energy is dissipated, primarily through internal damping mechanisms [85,86]. A delayed peak displacement relative to the peak force (Table 3), equal to 15.15 ms, underscores the importance of inertia effects, which resist instantaneous deformation. To highlight the contribution of inertia, a parameter ρ is introduced:

$$\rho = \frac{m_i \dot{u}_1 (t = 0)}{(m_i + m_{eq}) \max \dot{u}_2}. \tag{13}$$

It represents the ratio between the momentum of the impacting body and beam (thanks to the equivalent mass). Thanks to the principle of conservation of momentum, the ratio should be one. Fig. 13 illustrates the values of the ratio for the three parametric analyses. The plots, related to the three different analyses, show that the value is smaller than one for the quasi-totality of the cases. The only cases in which the ratio is larger than one are those depicted in Fig. 13.c: for short beams $\rho \geq 1$, while for longer beams it

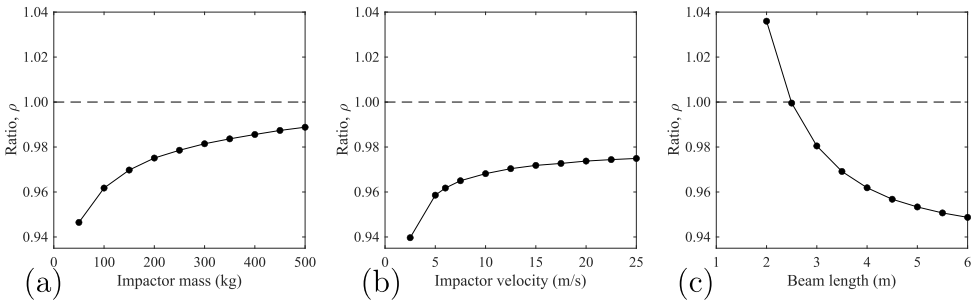

Fig. 13. Values of the parameter ρ highlighting the conservation of momentum at the instant in which the beam experiences the maximum velocity $\dot{u}_2$. Curve (a) refers to the different impacting masses analysis, curve (b) to the increasing impactor velocities, while curve (c) to the different beam lengths.

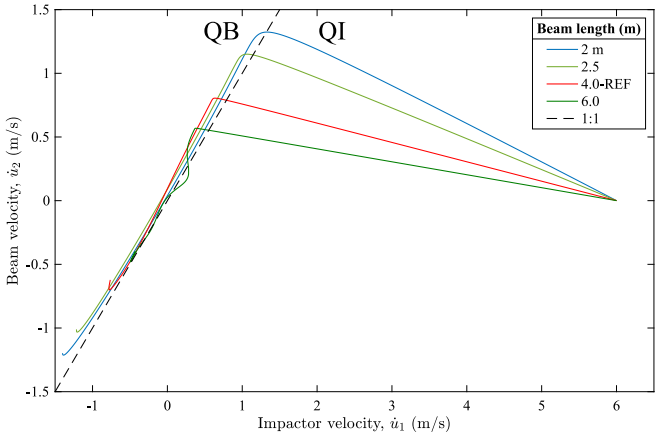

Fig. 14. Values of the velocity of the beam, $\dot{u}_2$, with respect to the velocity of the impacting mass, $\dot{u}_1$ for four different beam lengths, i.e. 2, 2.5, 4 and 6 m. The 1:1 dashed black curve indicates that impactor and beam have the same velocity.

turns smaller than one. To explain this odd behavior, it must be noted that the instant in which the beam experiences the maximum velocity $\dot{u}_2$, the impacting mass can have a different velocity $\dot{u}_1$, meaning that the indentation velocity $\dot{\delta}$ is different from zero.

Fig. 14 plots the values of the velocity of the beam, $\dot{u}_2$, with respect to the velocity of the impacting mass, $\dot{u}_1$ for four different beam lengths, i.e. 2, 2.5, 4 and 6 m. The graph reports the 1:1 dashed line that indicates that beam and impactor velocity have the same velocity. When the curves are situated on the right-hand side of the 1:1 line, the impactor moves quicker than the beam (QI case). On the contrary, when the curves lie on the left-hand side, the beam is quicker than the impactor (QB case). To achieve values of ρ larger than one, the maximum beam velocity should happen when the impactor has an equal velocity, i.e. when the maximum is on the 1:1 line. This clearly emerges for the 2 m blue curve and, roughly, for the 2.5 m case. On the contrary, for the remaining two cases, the maximum of $\dot{u}_2$ occurs when the beam has larger velocity than the mass, resulting in an overestimation of the momentum of the impactor, hence a larger value of the denominator of Eq. (13) resulting in a ratio smaller than one.

Regarding the influence of varying impactor mass, the observed lag between the peak contact force and the subsequent peak displacement is not solely due to inertial effects; it also reflects the influence of plasticity. In higher-mass impacts, the beam undergoes progressive irreversible deformation that reduces its effective stiffness, causing the rise of permanent deformations around the equilibrium point in the free-damped vibrations. Consequently, the redistribution of impact energy and the onset of permanent deformation both contribute to the extended time required to reach peak displacement. In the velocity-displacement plot (Fig. 7), the loops represent the dynamic trajectory of the beam's midspan velocity versus its displacement during the contact phase. For lower masses (m_i = 50 to 250 kg), the loops are compact, indicating that the beam undergoes relatively small deflections and rapid reversals of velocity, typical of an elastic response. In contrast, for higher masses (m_i = 350 to 500 kg), the loops are elongated, reflecting larger displacements and higher velocities that are associated with significant irreversible deformation and enhanced inertial effects.

In Fig. 8.a, the unloading paths deviate increasingly from the loading paths as mass increases, illustrating the transition from elastic to plastic deformation. For higher masses, larger loops highlight permanent deformation and greater energy dissipation. Fig. 8.b shows faster recovery for lower masses, with the beam's deflection decreasing more quickly after its peak, indicating a predominantly elastic behavior within the observed time window. In contrast, heavier masses exhibit larger deflections for a longer portion of the contact phase, indicating a greater tendency toward permanent deformations. As the impactor mass increases, the beam transitions from minimal residual deformation to fully irreversible behavior, with notable changes in key parameters such

as displacement, contact force, and energy dissipation. The results emphasize the importance of considering both reversible and irreversible responses when evaluating the dynamic performance and resilience of RC beams under impact loading.

The results demonstrate that initial velocity is a critical factor governing the beam's dynamic response, significantly influencing both the extent and the nature of structural damage. For example, increasing the initial velocity from 5 m/s to 25 m/s (a fivefold increase) results in more than ninefold increase in contact force and a fivefold increase in maximum deflection. Comparing this to the effect of mass, where a fivefold increase in mass resulted in a fivefold increase in deflection and only a 2.5-fold increase in contact force, it is evident that velocity has a more pronounced effect on contact force. This highlights the vulnerability of RC beams to sufficiently high-velocity impacts, which can aid in understanding dynamic failure propagation that may lead to progressive collapse.

Regarding the effect of beam length, the study reveals a fundamental design trade-off. This trend can be explained by the trade-off between stiffness and inertia, where inertia, which is defined as the product of mass and acceleration, plays a critical role under dynamic impact. Although in a purely static context, a beam with higher stiffness (as in shorter beams) would normally produce larger reactions for a given displacement, the larger distributed mass of longer beams increases their inertia, thereby limiting acceleration and allowing higher contact forces to develop before significant deformation occurs. For instance, the peak contact force for a beam of 2 m length is approximately 800 kN, whereas for a beam of 6 m length with lower stiffness, it exceeds 900 kN. This illustrates how mass-related inertia can outweigh the advantage of higher stiffness in short beams when subjected to fast, impulsive loads. Interestingly, at an early stage of the impact (e.g., $t = 5$ ms), longer beams show smaller deflections compared to shorter beams. This counterintuitive trend can be attributed to the greater equivalent mass of longer beams, resulting in higher inertia resistance. This inertia limits the deflection during the initial stages of impact. This behavior is further corroborated by Fig. 12, where the velocity-deflection loops for longer beams are wider and more pronounced, indicating greater energy dissipation through plasticity of the beam. Shorter beams, on the other hand, exhibit more compact loops, reflecting their higher stiffness and limited energy dissipation.

Crucially, the findings from the effect of different beam lengths on the dynamic response of RC beams underscore a fundamental design trade-off: shorter beams, with their higher stiffness but lower mass and inertia, are less effective at resisting dynamic impact forces during the initial stages of impact. Their limited ability to absorb energy increases their susceptibility to localized and brittle failure. Conversely, longer beams, with greater mass and inertia, resist deformation more effectively during the initial stages of impact. This resistance, combined with their flexibility, allows for greater energy absorption and more ductile deformation. However, this comes at the cost of larger deflections and an increased risk of progressive collapse.

A comparison showed that for impactor masses between 50 kg and 500 kg, the discrepancy between the Hertzian model and the current study consistently remains around 50%. This highlights the overestimation of contact forces by the Hertzian model when compared to the current study, particularly as the mass increases. In contrast, Yong's approach [28] aligns well under low-impact conditions (*e.g.*, masses $\leq$ 200 kg and velocities $\leq$ 10 m/s) but deviates by up to 17% for high-energy impacts. This indicates that Yong's model aligns more closely with the current study under conditions where impact forces are moderate and material deformation remains primarily elastic, with minimal plastic effects. Anyway, the obtained results highlight that it is necessary to consider the nature (beam, instead of half-infinite plane) and the corresponding deformability of the target when computing the collision force.

As the system transitions into the plastic regime, the deviations between the models increase significantly. This is particularly evident for cases involving higher mass and velocity, where the differences in maximum contact force between Yong's model and the current study become more pronounced, as seen in the last column of Table 4. This shift occurs due to increasing impact forces that exceed the material's elastic limit, leading to permanent deformations. Unlike Yong's approach, which primarily captures elastic and viscoelastic behavior, the compliance curve used in this study dynamically adjusts to the evolving stiffness of the beam, incorporating plastic deformation effects, making it more accurate in modeling high-impact cases.

The observed trends suggest that while the Hertzian and Yong's models provide reasonable approximations of the collision force under certain conditions, their accuracy diminishes as the contact scenario involves higher energy impacts. The current study captures these effects more accurately, especially in plastic deformation regimes, thereby providing a more reliable representation of the contact force behavior across a range of impact scenarios.

Validating the proposed model against experimental work by Fujikake et al. [27] shows a discrepancy of less than 2%, confirming the model's reliability. By comparing the proposed model with traditional approaches, the study demonstrated its superiority in accurately predicting structural responses, particularly in the plastic deformation phase. The model's ability to account for real-time mass redistribution and energy dissipation effects further enhances its applicability in designing impact-resistant structures.

6. Conclusions

This study presents an analytical model for predicting the dynamic response of RC beams under impact loads. The model has potential applications in assessing debris impact, contributing to a better understanding of pancake-type progressive collapse. By incorporating a dynamically recalculated equivalent mass and the Hunt–Crossley contact force model, the proposed framework provides unprecedented accuracy in capturing real-time interactions between the impacting body and the structure. Unlike traditional models that rely on fixed equivalent mass assumptions, this approach dynamically adapts to the beam's deformation profile, offering deeper insights into energy transfer, contact forces, and structural behavior under extreme loading conditions.

The proposed dynamic recalculation of m_{eq} during the simulation continuously updates the equivalent mass, ensuring a more precise representation of the beam's response as it transitions between elastic and plastic deformation. This dynamic approach allows

for a more accurate prediction of the beam's behavior under real-world impact conditions, particularly for scenarios involving large deformations or complex load cases. In addition, the step-by-step adjustment of both the equivalent mass and stiffness effectively captures complex structural behavior, including the transitions between elastic and plastic responses, as well as the unloading behavior and residual displacements that are critical for understanding structural performance during unloading phases.

The proposed analytical model relies on simplifying assumptions such as idealized stress–strain relationships, uniform material properties, and perfect bond conditions between concrete and reinforcement. In this analysis, shear failure is neglected by focusing solely on the beam's flexural response, and the dynamic recalculation of the equivalent mass and stiffness assumes that the beam's behavior can be fully captured by the pre-calculated compliance curve. This approach does not fully account for the complexities of inelastic deformation, strain rate effects, or additional dynamic phenomena that may occur at high impact velocities. Moreover, variations in experimental setups – such as differences in drop heights, impactor alignment, and support conditions – can introduce uncertainties that are not reflected in the model.

Future research on the analytical model should incorporate more comprehensive material characterization, consider additional failure modes (including shear), and examine a broader range of impact velocities and testing conditions to further refine the model's applicability and reliability. Extending the current studies on a simply supported beam subjected to an impact at its mid-span to more articulated scenarios, the future analyses should extend the model to system-level scale, incorporating interactions between structural elements and exploring multi-hazard scenarios. Experimental validation across diverse geometries and material properties would further strengthen its robustness. These advancements will pave the way for designing robust structures capable of withstanding impact-type progressive collapse, safeguarding critical infrastructure against catastrophic failure.

CRediT authorship contribution statement

Elahe Zeinali: Writing – review & editing, Writing – original draft, Visualization, Methodology, Formal analysis, Conceptualization. **Foad Kiakojouri:** Writing – review & editing, Methodology, Conceptualization. **Valerio De Biagi:** Writing – review & editing, Methodology, Formal analysis, Conceptualization.

Declaration of competing interest

The authors declare that they have no known competing financial interests or personal relationships that could have appeared to influence the work reported in this paper.

Data availability

Data will be made available on request.

References

[1] U. Starossek, Progressive Collapse of Structures, vol. 153, Thomas Telford London, 2009.
[2] S. Szyniszewski, Dynamic energy based method for progressive collapse analysis, in: Structures Congress 2009: Don't Mess with Structural Engineers: Expanding Our Role, 2009, pp. 1–10.
[3] F. Kiakojouri, M.R. Sheidaii, V. De Biagi, B. Chiaia, Progressive collapse of structures: A discussion on annotated nomenclature, Structures 29 (2021) 1417–1423.
[4] M. Guo, H. Huang, S. Yang, M. Huang, Experimental and numerical investigation on progressive collapse resistance of three-dimensional RC structures, Eng. Fail. Anal. 167 (2025) 108954.
[5] J.A. Pérez-Díaz, J.D. Ríos, E. Sánchez-González, A. Ponce-Torres, Analysis of the progressive collapse of a parking garage concrete structure due to punching shear, Eng. Fail. Anal. 167 (2025) 108902.
[6] F. Kiakojouri, V. De Biagi, M. Marchelli, B. Chiaia, A conceptual note on the definition of initial failure in progressive collapse scenarios, Structures 60 (2024) 105921.
[7] F. Kiakojouri, E. Zeinali, J.M. Adam, V. De Biagi, Experimental studies on the progressive collapse of building structures: A review and discussion on dynamic column removal techniques, Structures 57 (2023) 105059.
[8] H. Al-Thairy, Y. Wang, A numerical study of the behaviour and failure modes of axially compressed steel columns subjected to transverse impact, Int. J. Impact Eng. 38 (8–9) (2011) 732–744.
[9] C. Zeng, P. Cui, Z. Su, Y. Lei, R. Chen, Failure modes of reinforced concrete columns of buildings under debris flow impact, Landslides 12 (2015) 561–571.
[10] T.V. Do, T.M. Pham, H. Hao, Impact force profile and failure classification of reinforced concrete bridge columns against vehicle impact, Eng. Struct. 183 (2019) 443–458.
[11] S. Xiang, Y. He, T. Golea, V. Denoël, J.-F. Demonceau, Simplified methods to predict the robustness of steel parking-structure joints, J. Constr. Steel Res. 213 (2024) 108355.
[12] F. Yi, W.-J. Yi, J.-M. Sun, J. Ni, Q.-F. He, Y. Zhou, On the progressive collapse performance of RC frame structures under impact column removal, Eng. Struct. 307 (2024) 117926.
[13] L. Zheng, W.-D. Wang, M. Xiao, Y.-Q. Yu, H.-F. Sun, Bionic energy absorbers for parking structural columns against multi-angle vehicle collisions, J. Constr. Steel Res. 226 (2025) 109262.
[14] D. Kukla, A. Kozłowski, B. Miller, D. Ziaja, I. Wójcik-Grząba, S. Gubernat, Experimental study of innovative steel beam-to-column joint under impact loading to mitigate progressive collapse, J. Build. Eng. (2025) 112018.
[15] L.E.G. de Mattos, J.C.C.B. Carneiro, A.T. Beck, Risk-based optimum design of a device to simultaneously protect building columns against accidental impact, fire and progressive slab collapse, Eng. Struct. 332 (2025) 119983.
[16] F. Kiakojouri, V. De Biagi, Catenary mechanism in steel columns under extreme lateral loading: A basis for building progressive collapse analysis, Dev. Built Environ. 20 (2024) 100556.

[17] N. Lalkovski, U. Starossek, Vertical building collapse triggered by loss of all columns in the ground story- Last line of defense, Int. J. Steel Struct. 16 (2016) 395–410.
[18] N. Lalkovski, Progressive Collapse of High-Rise Buildings: Last Line of Defense (Ph.D. thesis), Mensch und Buch Verlag, 2022.
[19] H. Shakib, M. Pirizadeh, S. Dardaei, M. Zakersalehi, Technical and administrative assessment of Plasco building incident, Int. J. Civ. Eng. 16 (2018) 1227–1239.
[20] H. Shakib, M. Zakersalehi, V. Jahangiri, R. Zamanian, Evaluation of Plasco building fire-induced progressive collapse, in: Structures, vol. 28, Elsevier, 2020, pp. 205–224.
[21] L. Bredean, M. Botez, The influence of beams design and the slabs effect on the progressive collapse resisting mechanisms development for RC framed structures, Eng. Fail. Anal. 91 (2018) 527–542.
[22] D.Z. Yankelevsky, Y.S. Karinski, V.R. Feldgun, Damage and failure of a column-supported RC flat slab subjected to impulsive loading, Appl. Sci. 13 (3) (2023) 1933.
[23] C. Zhang, G. Gholipour, A.A. Mousavi, State-of-the-art review on responses of RC structures subjected to lateral impact loads, Arch. Comput. Methods Eng. 28 (4) (2021) 2477–2507.
[24] C. Yilmaz, O. Kirtel, G. Dok, A. Ilki, Experimental investigation on the post-impact behavior of normal-strength reinforced concrete beams subjected to drop-weight impact loads, Arab. J. Sci. Eng. 48 (10) (2023) 13241–13258.
[25] C. Baera, H. Szilagyi, C. Mircea, P. Criel, N. De Belie, Concrete structures under impact loading: general aspects, Urban. Archit. Constr./Urban. Arhit. Constr. 7 (3) (2016).
[26] R.Z. Al-Rousan, M.A. Alhassan, H. Al-Salman, Impact resistance of polypropylene fiber reinforced concrete two-way slabs, Struct. Eng. Mech. 62 (3) (2017) 373–380.
[27] K. Fujikake, B. Li, S. Soeun, Impact response of reinforced concrete beam and its analytical evaluation, J. Struct. Eng. 135 (8) (2009) 938–950.
[28] A.C. Yong, N.T. Lam, S.J. Menegon, Collision Actions on Structures, CRC Press, 2022, http://dx.doi.org/10.1201/9781003133032.
[29] S. Heimbs, S. Heller, P. Middendorf, F. Hähnel, J. Weiße, Low velocity impact on CFRP plates with compressive preload: test and modelling, Int. J. Impact Eng. 36 (10–11) (2009) 1182–1193.
[30] N. Kishi, S.G. Khasraghy, H. Kon-No, Numerical simulation of reinforced concrete beams under consecutive impact loading, ACI Struct. J. 108 (4) (2011) 444.
[31] J. Ožbolt, A. Sharma, Numerical simulation of reinforced concrete beams with different shear reinforcements under dynamic impact loads, Int. J. Impact Eng. 38 (12) (2011) 940–950.
[32] H. Thilakarathna, D. Thambiratnam, M. Dhanasekar, N. Perera, Numerical simulation of axially loaded concrete columns under transverse impact and vulnerability assessment, Int. J. Impact Eng. 37 (11) (2010) 1100–1112.
[33] S.D. Adhikary, B. Li, K. Fujikake, Low velocity impact response of reinforced concrete beams: experimental and numerical investigation, Int. J. Prot. Struct. 6 (1) (2015) 81–111.
[34] Z. Peilin, Y. Songhong, W. Junshun, et al., Analysis of dynamic response and impact resistance of corrugated plate-reinforced concrete under simulated rockfall, Eng. Fail. Anal. 167 (2025) 108922.
[35] D.-K. Thai, S.-E. Kim, Failure analysis of reinforced concrete walls under impact loading using the finite element approach, Eng. Fail. Anal. 45 (2014) 252–277.
[36] R.U.N. Dar, P. Alagappan, Ballistic impact response of reinforced concrete panels subjected to diverse multiple projectile impact scenarios: A numerical study, Eng. Fail. Anal. 164 (2024) 108697.
[37] J.S. Kwan, E.H. Sze, C. Lam, Finite element analysis for rockfall and debris flow mitigation works, Can. Geotech. J. 56 (9) (2019) 1225–1250.
[38] C. Grunwald, A.A. Khalil, B. Schaufelberger, E.M. Ricciardi, C. Pellecchia, E. De Iuliis, W. Riedel, Reliability of collapse simulation–Comparing finite and applied element method at different levels, Eng. Struct. 176 (2018) 265–278.
[39] Z. Zheng, Y. Tian, Z. Yang, X. Lu, Hybrid framework for simulating building collapse and ruin scenarios using finite element method and physics engine, Appl. Sci. 10 (12) (2020) 4408.
[40] P. Kœchlin, S. Potapov, Classification of soft and hard impacts—Application to aircraft crash, Nucl. Eng. Des. 239 (4) (2009) 613–618.
[41] N. Matos, M. Gomes, V. Infante, Numerical modelling of soft body impacts: A review, Eng. Fail. Anal. (2023) 107595.
[42] S. Saatcı, Structures Subjected to Impact Loads (Ph.D. thesis), University of Toronto, 2007.
[43] P. Bischoff, S. Perry, J. Eibl, Contact force calculations with a simple spring-mass model for hard impact: a case study using polystyrene aggregate concrete, Int. J. Impact Eng. 9 (3) (1990) 317–325.
[44] K.H. Hunt, F.R.E. Crossley, Coefficient of restitution interpreted as damping in vibroimpact, J. Appl. Mech. 42 (2) (1975) 440–445.
[45] A. Dancygier, Scaling of non-proportional non-deforming projectiles impacting reinforced concrete barriers, Int. J. Impact Eng. 24 (1) (2000) 33–55.
[46] A.N. Dancygier, D.Z. Yankelevsky, C. Jaegermann, Response of high performance concrete plates to impact of non-deforming projectiles, Int. J. Impact Eng. 34 (11) (2007) 1768–1779.
[47] Q. Li, X. Chen, Dimensionless formulae for penetration depth of concrete target impacted by a non-deformable projectile, Int. J. Impact Eng. 28 (1) (2003) 93–116.
[48] M. Zhang, V. Shim, G. Lu, C. Chew, Resistance of high-strength concrete to projectile impact, Int. J. Impact Eng. 31 (7) (2005) 825–841.
[49] M. Yamamoto, H. Masuya, Y. Nishimura, A study on the impact test method and characteristics of impact behavior of various reinforced concrete beams, in: Proc., 1st Int. Con. on Design and Analysis of Protective Structure against Impact/Impulsive/Shock Loads, DAPSIL Tokyo, 2003, pp. 245–255.
[50] N. Kishi, K. Ikeda, H. Mikami, E. Yamaguchi, Dynamic behavior of RC beams under steel weight impact loading. Effects of nose-shape of steel weight, in: Third International Conference on Concrete under Severe Conditions, CONSEC'01, 2001, pp. 660–667.
[51] N. Kishi, T. Ando, K. Imoto, M. Ishida, Y. Kasai, S. Katsuki, A. Kanbayashi, H. Masuya, Round robin analysis of RC beam subjected to an impact load due to a falling weight, in: Proc., 1st Int. Conf. on Design and Analysis of Protective Structure Against Impact/Impulsive/Shock Loads, DAPSIL Tokyo, 2003, pp. 305–318.
[52] G. Hughes, A. Beeby, Investigation of the effect of impact loading on concrete beams, Struct. Eng. B 60 (1982) 45–52.
[53] N. Ishikawa, S. Katsuki, K. Takemoto, Dynamic analysis of prestressed concrete beams under impact and high speed loadings, WIT Trans. Built Environ. 48 (2000).
[54] M. D'Antimo, M. Latour, G. Rizzano, J.-F. Demonceau, Experimental and numerical assessment of steel beams under impact loadings, J. Constr. Steel Res. 158 (2019) 230–247.
[55] T.M. Pham, H. Hao, Effect of the plastic hinge and boundary conditions on the impact behavior of reinforced concrete beams, Int. J. Impact Eng. 102 (2017) 74–85.
[56] S. Shi, L. Zhu, T. Yu, Dynamic modelling of elastic-plastic beams under impact, Int. J. Impact Eng. 126 (2019) 1–10.
[57] Y.A. Rossikhin, M.V. Shitikova, Classical beams and plates in a fractional derivative medium, impact response, in: Encyclopedia of Continuum Mechanics, Springer, 2020, pp. 294–305.
[58] T.M. Pham, H. Hao, Influence of global stiffness and equivalent model on prediction of impact response of RC beams, Int. J. Impact Eng. 113 (2018) 88–97.
[59] N.M. Woodhouse, One degree of freedom, in: Introduction to Analytical Dynamics: Revised Edition, Springer, 2009, pp. 35–66.
[60] J. Sun, N. Lam, L. Zhang, D. Ruan, E. Gad, Computer simulation of contact forces generated by impact, Int. J. Struct. Stab. Dyn. 17 (01) (2017) 1750005.

[61] K. Wu, T. Yu, Simple dynamic models of elastic–plastic structures under impact, Int. J. Impact Eng. 25 (8) (2001) 735–754.
[62] H. Li, W. Chen, T.M. Pham, H. Hao, Analytical and numerical studies on impact force profile of RC beam under drop weight impact, Int. J. Impact Eng. 147 (2021) 103743.
[63] A. Ventura, V. De Biagi, B. Chiaia, Effects of rockfall on an elastic-plastic member: A novel compliance contact model and dynamic response, Eng. Struct. 148 (2017) 126–144.
[64] H. Hertz, The contact of elastic solids, J. Reine Angew. Math. 92 (1881) 156–171.
[65] A.C. Fischer-Cripps, Introduction to Contact Mechanics, vol. 101, Springer, 2007.
[66] W. Thomson, IV. On the elasticity and viscosity of metals, Proc. R. Soc. Lond. (14) (1865) 289–297.
[67] W. Voigt, Ueber innere Reibung fester Körper, insbesondere der Metalle, Ann. Phys., Lpz. 283 (12) (1892) 671–693.
[68] J. Sun, N. Lam, L. Zhang, D. Ruan, E. Gad, Contact forces generated by hailstone impact, Int. J. Impact Eng. 84 (2015) 145–158.
[69] S. Shi, N. Lam, S. Chen, Y. Cui, G. Lu, E. Gad, L. Zhang, An analytical approach for modelling contact forcing function of hailstone impact, Int. J. Solids Struct. 269 (2023) 112214.
[70] M.R. da Silva, F. Marques, M.T. da Silva, P. Flores, A compendium of contact force models inspired by Hunt and Crossley's cornerstone work, Mech. Mach. Theory 167 (2022) 104501.
[71] P. Heng, Simplified mechanical models for the Nonlinear Dynamic Analysis of Elasto-Plastic Steel Structures Impacted by a Rigid Body (Ph.D. thesis), KTH Royal Institute of Technology, 2017.
[72] H. Ghaednia, X. Wang, S. Saha, Y. Xu, A. Sharma, R.L. Jackson, A review of elastic–plastic contact mechanics, Appl. Mech. Rev. 69 (6) (2017) 060804.
[73] H.M. Lankarani, P. Nikravesh, A contact force model with hysteresis damping for impact analysis of multibody systems, in: International Design Engineering Technical Conferences and Computers and Information in Engineering Conference, vol. 3691, American Society of Mechanical Engineers, 1989, pp. 45–51.
[74] Y. Wang, Q. Peng, H. Song, Y.-G. Wei, X. Liu, Semi-analytical model for elastoplastic impact of sphere on plate, Int. J. Impact Eng. (2025) 105229.
[75] E. Sánchez, A. Cosimo, O. Brüls, A. Cardona, F.J. Cavalieri, Simulation of impacts between spherical rigid bodies with frictional effects, Internat. J. Numer. Methods Engrg. 125 (20) (2024) e7556.
[76] M. Wu, C. Zhang, Z. Chen, Drop-weight tests of concrete beams prestressed with unbonded tendons and meso-scale simulation, Int. J. Impact Eng. 93 (2016) 166–183.
[77] T.M. Pham, H. Hao, Impact behavior of FRP-strengthened RC beams without stirrups, J. Compos. Constr. 20 (4) (2016) 04016011.
[78] T.M. Pham, H. Hao, Behavior of fiber-reinforced polymer-strengthened reinforced concrete beams under static and impact loads, Int. J. Prot. Struct. 8 (1) (2017) 3–24.
[79] N. Kishi, H. Mikami, Empirical formulas for designing reinforced concrete beams under impact loading, ACI Struct. J. 109 (4) (2012).
[80] S. Saatci, F.J. Vecchio, Effects of shear mechanisms on impact behavior of reinforced concrete beams, ACI Struct. J. 106 (1) (2009) 78.
[81] V. De Biagi, M. Marchelli, An experimental setup to study the collision force between brittle impacting bodies, Int. J. Impact Eng. 196 (2025) 105160.
[82] D. Bertrand, F. Kassem, F. Delhomme, A. Limam, Reliability analysis of an RC member impacted by a rockfall using a nonlinear SDOF model, Eng. Struct. 89 (2015) 93–102.
[83] Z.Z. Majeed, N.T. Lam, C. Lam, E. Gad, J.S. Kwan, Contact force generated by impact of boulder on concrete surface, Int. J. Impact Eng. 132 (2019) 103324.
[84] The MathWorks, Inc., MATLAB, Version R2024a, The MathWorks, Inc., Natick, Massachusetts, 2024, Available: https://www.mathworks.com.
[85] J. Zhang, W. Li, L. Zhao, G. He, A continuous contact force model for impact analysis in multibody dynamics, Mech. Mach. Theory 153 (2020) 103946.
[86] M. Sakai, Energy principle of the indentation-induced inelastic surface deformation and hardness of brittle materials, Acta Met. Mater. 41 (6) (1993) 1751–1758.